ADVANCED MATERIALS
www.advmat.de

Optically Tunable Electrical Oscillations in Oxide-Based Memristors for Neuromorphic Computing

Shimul Kanti Nath, Sujan Kumar Das, Sanjoy Kumar Nandi,* Chen Xi, Camilo Verbel Marquez, Armando Rúa, Mutsunori Uenuma, Zhongrui Wang, Songqing Zhang, Rui-Jie Zhu, Jason Eshraghian, Xiao Sun, Teng Lu, Yue Bian, Nitu Syed, Wenwu Pan, Han Wang, Wen Lei,* Lan Fu, Lorenzo Faraone, Yun Liu, and Robert G. Elliman*

The application of hardware-based neural networks can be enhanced by integrating sensory neurons and synapses that enable direct input from external stimuli. This work reports direct optical control of an oscillatory neuron based on volatile threshold switching in V_3O_5. The devices exhibit electroforming-free operation with switching parameters that can be tuned by optical illumination. Using temperature-dependent electrical measurements, conductive atomic force microscopy (C-AFM), in situ thermal imaging, and lumped element modelling, it is shown that the changes in switching parameters, including threshold and hold voltages, arise from overall conductivity increase of the oxide film due to the contribution of both photoconductive and bolometric characteristics of V_3O_5, which eventually affects the oscillation dynamics. Furthermore, V_3O_5 is identified as a new bolometric material with a temperature coefficient of resistance (TCR) as high as −4.6% K^{-1} at 423 K. The utility of these devices is illustrated by demonstrating in-sensor reservoir computing with reduced computational effort and an optical encoding layer for spiking neural network (SNN), respectively, using a simulated array of devices.

1. Introduction

Oscillatory neural networks provide a powerful platform for analogue computation and are of increasing interest as accelerators in artificial intelligence hardware, where they provide an energy-efficient means of undertaking simple repetitive functions such as calculating dot products, convolutions, applying nonlinearities, and recognizing or matching simple patterns. They also have the potential to undertake computationally hard problems that have no efficient solution on conventional computing platforms.[1] However, it is generally recognized that oscillator arrays based on conventional complementary metal-oxide-semiconductor (CMOS) circuits are too large and energy-consuming to enable integration into the dense, low-power arrays required for solving complex real-world problems. This has motivated

S. K. Nath, S. Zhang, W. Pan, H. Wang, W. Lei, L. Faraone
Department of Electrical
Electronic and Computer Engineering
The University of Western Australia
35 Stirling Highway, Perth, WA 6009, Australia
E-mail: shimul_kanti.nath@unsw.edu.au; wen.lei@uwa.edu.au

S. K. Nath, S. K. Das, S. K. Nandi, Y. Bian, L. Fu, R. G. Elliman
Department of Electronic Materials Engineering
Research School of Physics
The Australian National University
Canberra, ACT 2601, Australia
E-mail: sanjoy.nandi@anu.edu.au

The ORCID identification number(s) for the author(s) of this article can be found under https://doi.org/10.1002/adma.202400904

DOI: 10.1002/adma.202400904

S. K. Nath
School of Photovoltaic and Renewable Energy Engineering
University of New South Wales (UNSW Sydney)
Kensington, NSW 2052, Australia

S. K. Das
Department of Physics
Jahangirnagar Univeristy
Savar, Dhaka 1342, Bangladesh

C. Xi, Z. Wang
Department of Electrical and Electronic Engineering
the University of Hong Kong
Pok Fu Lam Rd, Hong Kong Island Hong Kong

C. V. Marquez, A. Rúa
Department of Physics
University of Puerto Rico
Mayaguez, PR 00681, USA

M. Uenuma
Information Device Science Laboratory
Nara Institute of Science and Technology (NAIST)
Nara 630-0192, Japan

a recent interest in the development of alternative nanoscale oscillators based on phase-change materials, spintronics (i.e., spin-torque and spin-Hall oscillators), nano-electro-mechanical systems (NEMS), superconducting devices (e.g., Josephson junctions), and materials that exhibit volatile memristive switching or negative differential resistance (NDR).[2]

Among the various contenders, relaxation oscillators based on NDR or threshold switching in metal-oxide-metal (MOM) devices are of particular interest due to their simple structure, scalability, and energy efficiency.[3] When two or more such oscillators are appropriately coupled, they form a simple neuristor circuit that can be used to emulate the basic functions of a biological neuron.[4] Hopfield neural networks can be developed by replacing neurons with oscillators and synapses with coupling resistors or capacitors.[5] Such networks can be trained for image recognition by tuning the coupling strength (resistor or capacitor).[5a]

NDR or threshold switching has been reported in a wide range of oxides (e.g., SiO_x, TiO_x, TaO_x, VO_x, NbO_x) and other materials but devices typically require an electroforming step to initiate this response. This involves subjecting the oxide to electrical stress to induce soft dielectric breakdown, a process that creates a localized conductive path through the oxide film.[5b] The stochastic nature of this process, including uncontrolled current overshoot during dielectric breakdown, causes significant device variability. As a consequence, it is difficult to predict the response of a given device in advance, with many exhibiting nonvolatile resistance changes due to the generation, drift and diffusion of point defects (e.g., oxygen vacancies), or a combination of volatile and nonvolatile resistive switching.[5b,6] Devices based on vanadium and niobium oxides have proven to be the most predictable in this regard and are the most widely studied.[4a,6b,7]

One of the reasons the vanadium and niobium oxides are of interest is that they have phases (i.e., VO_2 and NbO_2) that undergo insulator to metal transitions (IMT) above room temperature,[8] and these produce large conductivity changes over a narrow temperature range, which is ideal for fabricating low power relaxation oscillators.[6b,9] However, despite its widespread use as a prototypic material, the transition temperature of VO_2 (i.e., T_c = 340 K) is too low for applications requiring large-scale integration, while that of NbO_2 (≈1080 K) is so high that the NDR is generally dominated by Poole–Frenkel conduction at temperatures well below the transition temperature (i.e., ≈600 K). They also typically require an electroforming step as mentioned above, affecting their reliability for practical application. Unfortunately, there are very few binary metal-oxides with IMT temperatures above room temperature, but one important exception is V_3O_5.[9a] It is one of a series of vanadium-oxide Magnéli phases, and one of only two vanadium oxides that undergo IMT above room temperature (T_c = 430 K).[9a] However, even in this case the NDR response is dominated by Poole-Frenkel conduction and occurs at temperatures below the IMT temperature.[6b,10]

The NDR response of MOM devices is determined by the increase in oxide conductivity due to local Joule heating, and therefore depends on the total current and its distribution within the device. Thus, there is a great interest in tuning the magnitude or distribution of the current by external stimuli leading to engineered device characteristics with multifunctionalities. One approach in this regard can be the employment of combined electric field and optical illumination to tune the NDR response and oscillation dynamics (or spike firing rate) when configured in neural networks. Using an applied voltage provides a means of compensating for device nonuniformity or optimizing computation, while the ability to modify the oscillator dynamics using light-exposure provides the basis for making an oscillatory SNN with direct optical input, useful for applications such as image segmentation or machine vision.

The utility of photogating has been shown for nonvolatile memristive switching devices[11,12] and to make photosensitive synapses for neural networks,[6a,13] and only a few recent studies have reported the feasibility of a photosensitive oscillator, which was, however enabled by the integration of a separate photodiode in the oscillator circuit[14,7b] The requirement of an external photodiode increases material consumption and processing time, which adds to the processing cost and complicates integration with the memristor technology. There are currently inadequate reports on direct optical control of oscillators based on the intrinsic photoresponse of the memristor that could potentially address these shortcomings. This scarcity is primarily due to the challenge in identifying suitable material systems that reliably exhibit volatile threshold switching while responding to optical stimuli.

In this study, by using polycrystalline V_3O_5 film as the functional oxide film, we report direct optical control of device response and electrical spikes in a two-terminal planar structure which shows robust memristive switching characteristics. Specifically, we present physical, optical, and electrical properties of V_3O_5 with an emphasis on their threshold switching response and show that the switching parameters can be engineered by the wavelength and intensity of the incident light. Using temperature-dependent electrical measurements, in situ thermal imaging and lumped element modeling, we show that the conductivity of the oxide film increases due to photoconductive and bolometric effects, which in turn affects the device

R.-J. Zhu, J. Eshraghian
Department of Electrical and Computer Engineering
University of California
Santa Cruz, CA 95064, USA
X. Sun
John de Laeter Centre
Curtin University
Perth, WA 6102, Australia
T. Lu, Y. Liu
Research School of Chemistry
The Australian National University
Canberra, ACT 2601, Australia
Y. Bian, L. Fu
Australian Research Council Centre of Excellence for Transformative Meta-Optical Systems
Canberra, ACT 2601, Australia
N. Syed
Australian Research Council Centre of Excellence for Transformative Meta-Optical Systems, School of Physics
University of Melbourne
Melbourne, Victoria 3010, Australia
W. Pan, L. Faraone
Australian Research Council Centre of Excellence for Transformative Meta-Optical Systems
Perth, WA 6009, Australia

response and oscillation dynamics. Additionally, the utility of spike frequency tuning by an optical means is demonstrated by simulating an array of devices that is capable to perform image segmentation tasks.

2. Results and Discussions

2.1. Thin Film Analysis

The crystal structure of the oxide films was initially investigated by XRD, and Rietveld refinement of the diffraction pattern confirmed that polycrystalline monoclinic V_3O_5 films ($P_{2/c}$ space group (JCPDS card 72–0977)[9a]) were achieved by sputter deposition. SEM and AFM measurements identified a granular distribution of crystallites and a rough surface with a rms roughness of around 24.65 ± 1.35 nm. Results of these analyses have been reported in our previous study.[6b]

FTIR transmittance and UV–Visible absorption spectra of the as-deposited film were measured within the wavelength range of 1.5 to 10 µm and 200 to 1500 nm, respectively. **Figure 1a** shows a Tauc plot derived from the FTIR data indicating the optical bandgap of V_3O_5 film. The extracted bandgap energy is ≈0.55 eV, similar to that of VO_2 and consistent with the previous report for V_3O_5.[15] From Figure 1b, it is evident that the film had a broad absorption ranging from UV–Visible to near-infrared with a peak absorption at around 400 nm followed by a dip at around 600 nm. Following that, the absorption increases monotonically with increasing wavelengths within the range 600 nm ≤ λ ≤ 1500 nm. In this context, we note that XPS spectra of as-deposited films showed contributions from different valence states of vanadium (see Figure S1, Supporting Information) which might influence the overall optical absorption.

The electrical properties of the V_3O_5 film and their role in determining the device characteristics were assessed by measuring the film resistivity using 4-point probe contacts in a van der Pauw configuration. The measurements were performed over the temperature range of 343–478 K under both dark and illumination conditions as shown in Figure S2a (Supporting Information). This temperature range was chosen because VO_2 exhibits IMT at around 340 K and shows near-metallic conductivity above this temperature. Under both dark and light conditions, the resistivity was found to decrease monotonically with increasing temperature between 343 and 420 K (i.e., on set of IMT), and to decrease by an order of magnitude at temperatures between 423 and 443 K, consistent with the expected IMT in the V_3O_5 phase.[6b,9a] The effect of white light illumination on the film resistivity is shown in Figure 1d, showing a decrease in resistivity for temperatures below or near IMT and no significant change for higher temperatures. This clearly shows that the film is more sensitive to light illumination when it is in its insulating state than when it is in its metallic state, as expected. Similar results were obtained when the film was illuminated with monochromatic laser sources (see Figure S2b, Supporting Information).

Conductive atomic force microscopy (C-AFM) mapping of the V_3O_5 film shows that the conductivity and photoinduced conductivity is heterogenous. Figure 1e shows room temperature 2D maps of through film current distributions measured using a dc bias voltage of 4 V. Under dark conditions, most regions of the film present low conductivity and only few grains (especially

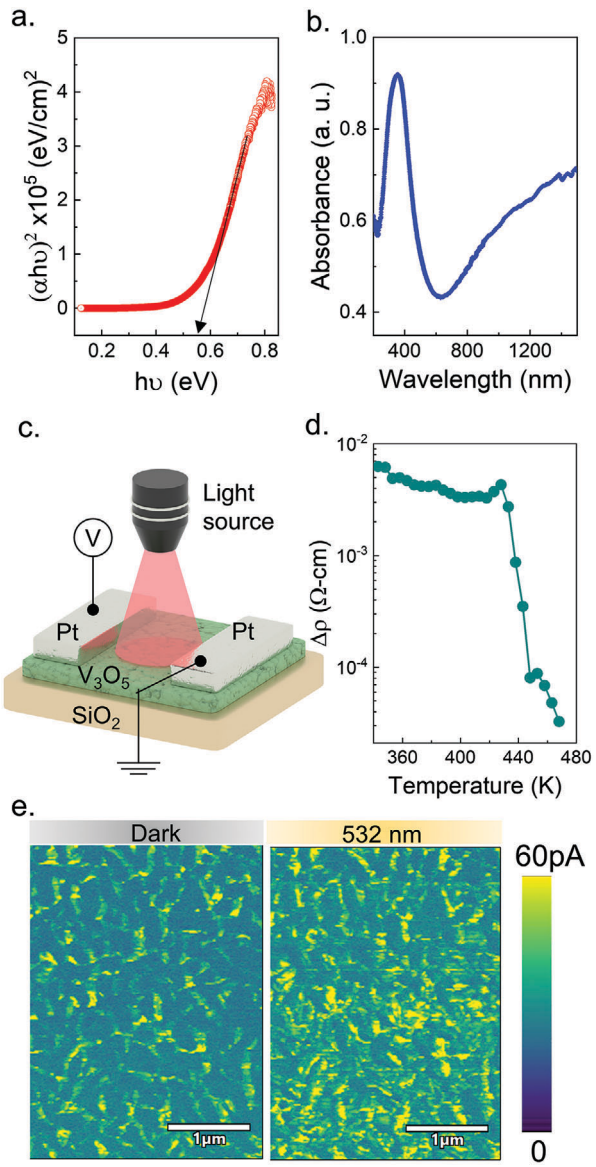

Figure 1. a) Tauc plot (using FTIR data) showing the optical band gap of the film, b) UV–Visible absorption spectra. c) Schematic of the device structure when illuminated with a light source, d) difference of film resistivity measured under dark and white light illumination ($\Delta\rho = \rho_{Dark} - \rho_{Light}$) as a function of stage temperature, and e) conductive atomic force microscopy (C-AFM) of the film under dark and illumination with a 532 nm laser.

the grain boundary regions) have the dominant current response. However, under illumination with a 532 nm laser light, the number of conductive grains increases, consistent with an increase in overall film conductivity. Further insights into the light-induced conductivity increase are provided in the subsequent sections.

The wide spectral absorption range, from visible to near-IR, and the photoinduced conductivity change of the V_3O_5 film indicate its potential for application in photoresponsive devices. After depositing the Pt electrodes, we tested the current-voltage (I-V) and current-time (I-t) characteristics (at a fixed voltage) of the device structure as shown schematically in Figure 1c, where V_3O_5 film serves as the functional layer.

2.2. Photogated Memristive Switching Response of Two Terminal Metal-V_3O_5-Metal Structures

Figure 2a shows representative quasi-static *I–V* characteristics of a two terminal V_3O_5 device (gap distance between the two electrodes ≈5 µm) measured under voltage-controlled testing with variable illumination. Under dark condition, the device exhibited symmetric threshold switching and NDR with a threshold voltage (V_{TH}) of around 1.13 V (indicated by the black line in the bottom panel of Figure 2a). The dependence of the threshold and hold voltages on the electrode gap can be found elsewhere.[6b] Significantly, these devices do not require an electroforming step to initiate the threshold switching response, a feature that is reflected in their excellent uniformity and reliability (i.e., cycle-to-cycle variation (<5%)) (see Figure S2c, Supporting Information).

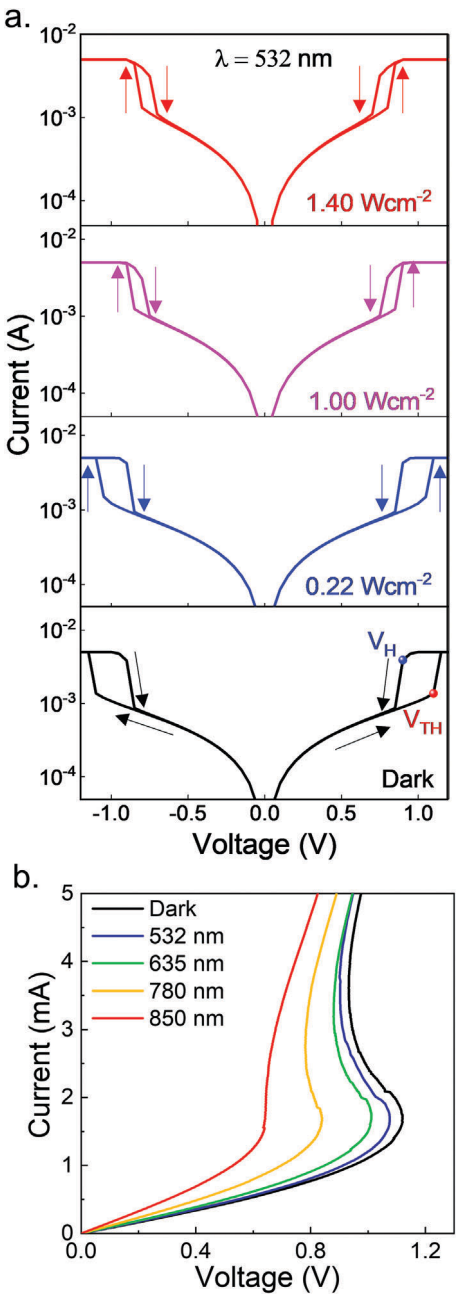

Figure 2. a) Threshold switching characteristics as a function of light intensity for illumination with 532 nm laser and b) light-wavelength dependent tuning of negative differential resistance (NDR) (laser power density: 0.22 W cm^{-2}).

The photoresponse of the device was investigated by illuminating the active device area with a 532 nm laser. As shown in Figure 2, this increased the conductivity of the oxide layer and had a significant effect on the switching characteristics. The latter include a reduction in the threshold and hold voltages with increasing laser intensity (Figure 2a) and a concomitant reduction in the hysteresis window. These effects were also found to depend on the incident laser wavelength, as evident from the current-controlled NDRs measured under visible and near-IR laser illumination (Figure 2b). Further examples of laser intensity dependent NDR and wavelength-dependent threshold switching are given in Figure S3 (Supporting Information). Such data clearly show direct optical control of threshold switching or NDR response using visible to near-IR illumination.

To examine the reliability of devices under illumination the dc endurance characteristics of a device with V_{TH} = 1.2 V was measured by illuminating it with a 780 nm laser. Quasi-static *I–V* measurements were performed in the dark and under illumination for 60 consecutive cycles and the device exhibited negligible cycle-to-cycle variability (see Figure S4, Supporting Information). The device-to-device variability of threshold parameters was reported in our earlier study[6b] and is not reproduced in this paper. However, we note that the magnitude of threshold hysteresis reduction upon illumination depends on several factors, including the wavelength and intensity of light and the distance between the two electrodes (see Figures S3 and S5, Supporting Information). The light-controlled reduction was similar for devices with similar electrode gaps but was more prominent for large-gap devices with higher threshold and hold voltages (Figure S5, Supporting Information).

Compositional analysis after electrical measurements using ToF-SIMS (see Figure S6, Supporting Information) showed no discernible difference between the V_3O_5 film in the active device area and that in the surrounding area (with a lateral resolution of 100 nm), confirming the stability of the devices under repeated cycling and illumination.

2.3. Photoresponse Mechanism

Figure 3a shows the room temperature photocurrent (*I–t* curves) for a two-terminal device as a function of laser power density (laser wavelength, λ = 532 nm) with a constant bias voltage of 500 mV. The laser light source was turned on and off every 40 s, and the photoresponse times (rise and fall times) were measured using an oscilloscope, as shown in Figure 3b. The rise and fall times were defined as the time taken for the current to increase or decrease within the range from 10% to 90% of the current maximum value or vice versa, respectively, and the observed millisecond transition times are similar to that reported for VO_2-based devices.[7]

The broadband photoresponse of the device was investigated by recording I-t curves for different laser wavelengths

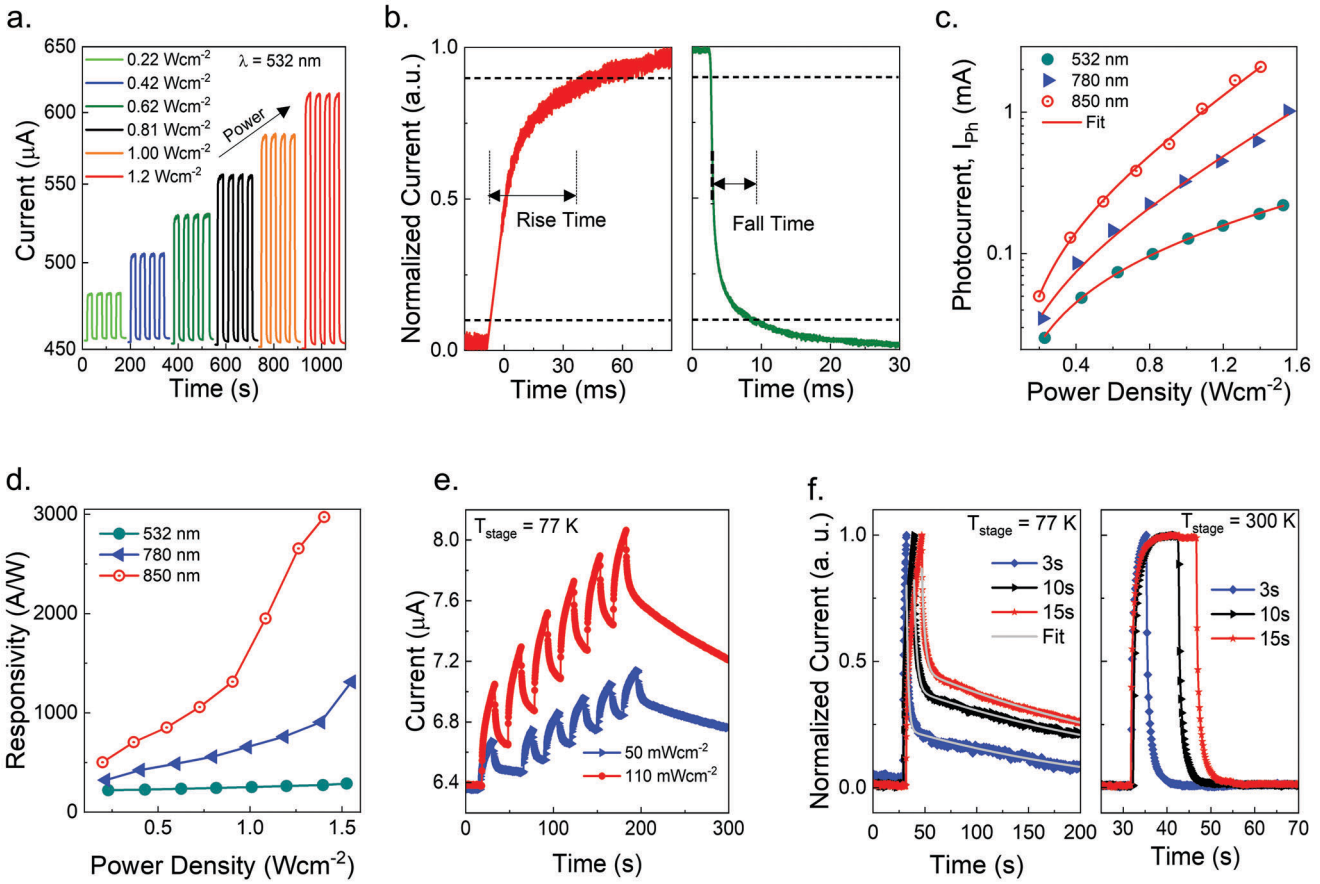

Figure 3. a) Light-induced increase of device current as a function of laser power density with 40 s light ON/OFF time at a constant bias of 0.5 V, b) photoresponse time, c,d) extracted photo current and responsivity as function of wavelength and light intensity. The data in Figure 3a–d were obtained from measurements performed at room temperature. e) Dynamical photocurrent response at a constant bias of 0.5 V with consecutive 15 s light ON/OFF time at a stage temperature of 77 K, and f) comparison of photocurrent decay time as a function of exposure time at two distinct stage temperatures.

(from 532 nm to 850 nm) and power densities. Using these data, the magnitude of photocurrent, defined as the difference between the maximum laser on current and dark current ($I_{Ph} = I_{laser\ on} - I_{laser\ off}$), was estimated. As shown in Figure 3c, the photocurrent exhibited a clear dependence on both laser wavelength and power density, with an exponential dependence on power density evident at higher power densities. The responsivity (R) of the photoconductor was defined as $R = I_{Ph}/(P \times S)$, where, P is the incident power intensity of the laser beam, and S is the active device area, and is shown in Figure 3d (specific detectivity of the device is given Figure S7, Supporting Information). These data show that the device has a photoresponse in both visible and near-IR spectral range, with the relative response partly reflecting the increased photon flux at longer wavelengths (In a conventional photoconductor, at a fixed power density, photon flux is proportional to the wavelength). Significantly, the data in Figure 3c,d do not exhibit the linear trend expected for devices operating in photoconductive mode, but rather exhibit an exponential dependence similar to that observed for VO_2 devices,[6b] possibly due to additional contribution from photothermal (i.e., bolometric) effect.

In a two-terminal photoconductor device, the photoexcited carriers (electrons and holes) are separated by electric fields, and carrier mobility determines the transit time and speed of the device.[16] If the incident photon energy is larger than the bandgap energy of the semiconductor, the photogenerated carriers lose their extra energy by thermalization, which increases the local temperature. As a consequence, both photoelectric hot-carrier injection and photothermal hot carrier relaxation contribute to the broad-band photon-energy conversion, and their individual contributions can be distinguished by controlling the photon exposure time when conducting current–voltage measurements.[17]

To further investigate the photoresponse mechanism, time-resolved photoresponse measurements were performed on devices at different stage temperatures while illuminated with a 780 nm laser light at a fixed bias voltage of 500 mV. Figure 3e shows the photocurrent measured during six consecutive illumination cycles when cooled down to 77 K, in which the illumination was turned on and off every 15 s. The device current remains invariant prior to illumination (see the data for 1 to 15 s) but increases with a characteristic time constant when exposed to light and decreases with a similar time constant when the light is turned off. However, the current at the end of each cycle remains higher than that of the preceding cycle so that there is a gradual increase in photocurrent with increasing cycle number. The time taken to return to its initial state (dark current level) was found to depend on the laser power density and the duration of laser

Table 1. Extracted time constants as a function of exposure time.

Exposure time [s]	t_1 [s]	t_2 [s]
3	1.72 ± 0.028	233.45 ± 5.58
10	2.74 ± 0.029	261.74 ± 1.06
15	2.92 ± 0.03	266.24 ± 0.79

exposure as shown in Figure 3e,f. Figure 3f shows the photocurrent decay time as a function of laser exposure time when recorded for a single exposure cycle and fitted with a double exponential function of the form:

$$y = y_0 + A_1 e^{-\frac{x}{t_1}} + A_2 e^{-\frac{x}{t_2}} \quad (1)$$

where, $y_0$is offset, A_1 and A_2 are amplitudes and t_1 and t_2 are time constants (as shown in **Table 1**).

These data clearly highlight the existence of two distinct temporal regimes, one with a time constant t_1 of order of seconds, and a second with a longer time constant t_2 of order of a few minutes. Such behavior is typical of bolometric materials, in which the shorter time constant is attributed to photocarrier lifetime and the slow response to thermal relaxation effects.[18] Figure 3f compares the photocurrent response measured at 300 and 77 K, showing that the signature of bolometric effects is more prominent at low temperature, consistent with a relaxation of phonon modes when cooled down to low temperatures.

To gain further insight into the physical mechanism underpinning the electrical response of our device, in situ thermal imaging was performed under different environment and selected results are shown in **Figure 4**. The thermal imaging technique provides a powerful tool to understand the device characteristics, including redistribution and self-filamentation processes that result from changes in the local conductivity[5,19] Figure 4a shows the *I–V* characteristics of a 120 µm V_3O_5 device measured under dark and white light illumination at two different stage temperatures (303 and 333 K) and the Figure 4b shows the temperature profile extracted at the middle (halfway from both electrodes) of the device as a function of applied current. The corresponding temperature maps of Figure 4b are shown in Figure S8 (Supporting Information) at a stage temperature of 303 K.

The dark current temperature maps show that the current distribution gradually constricts with increasing operating current, and a filamentary conduction path (narrower than the electrode's width) clearly appears when the device is operated within (or above) the NDR region (i.e., ≥1.3 mA). This distribution becomes more localized when the operating current is further increased, and the filament temperature exceeds that of IMT at around 3.2 mA. Interestingly, the onset temperature of the threshold point (at 1.3 mA) is lower than the IMT temperature, showing that the NDR mechanism is dominated by local joule heating and gradual current constriction.[6] In this context, we note that, the S-type NDR in metal-oxide-metal devices can arise from any conduction mechanism in which the device conductivity shows a super-linear temperature dependence.[20] As such, the NDR response is determined by the increase in oxide conductivity due to local Joule heating, and therefore can be simulated with a lumped element model of NDR (see Supporting Information). Further details of the threshold switching mechanism can be found in our earlier study.[6b]

Of particular interest in the present study is the effect of light illumination on the device temperature and current distributions as shown in Figure 4b. Comparison of the temperature maps shows that below the NDR region, light exposure leads to an apparent increase of V_3O_5 film temperature. This is further quantified by performing same measurements under voltage-controlled testing on a similar device, as shown in Figure 4c–h. When exposed to white light, there was an increase in leakage current and a decrease in threshold voltage (Figure 4c), same as that observed before for monochromatic laser illumination (Figure 2a). Temperature maps were recorded while the device was biased with a constant bias voltage (e.g., 1, 12, and 16 V) as shown in Figure 4d. The average temperature within the active device region (i.e., area between the two electrodes) was estimated in relation to bias voltage and light intensity.

Figure 4e,f shows that under dark condition, the device current and corresponding surface temperature increases with increasing bias voltage, consistent with joule heating effect, and maintains a uniform profile during the whole period of voltage stress. The surface temperature returns quickly to room temperature (≈292 K) when the bias voltage is withdrawn. In contrast, upon light exposure, the device current and surface temperature (at 1 and 12 V) gradually rose with a characteristic time constant and then gradually returned to its initial temperature with a similar time constant after the light source was switched off. The time to return to the room temperature was found to depend on the applied voltage and light intensity as evident from Figure 4h where the device was biased with a higher voltage (16 V) near to the dark-condition threshold voltage ($V_{TH\ (dark)}$ = 17 V). In this case, exposure of light with 100% intensity led to an abrupt increase of temperature to 382 K (which was limited by the current compliance, as evident in Figure 4g), consistent with the fact that the device underwent filamentary conduction as the threshold voltage shifted below operating voltage (i.e., 16 V). Simultaneous withdrawal of voltage and light exposure caused lowering of temperature with an initial rapid decrease to dark-current temperature (temperature gradient indicated by ΔT_1) followed by a much slower decrease to room temperature (this temperature gradient is indicated by ΔT_2), consistent with two temporal regimes as discussed earlier.

These data clearly indicate that, V_3O_5 has a photothermal (bolometric) effect as reported for VO_2 and graphene,[7a,18b] in which the photogenerated carriers relax by transferring their energy to the lattice leading to a photoinduced reduction of film resistance.[7a,21] The initial decrease of film resistance has a significant effect on the local current distribution that ultimately affects the quasistatic volatile NDR characteristics, as also supported by LT Spice modelling (see Figures S9,S10, Supporting Information).

The bolometric performance of our device was investigated by performing temperature-dependent *I–V* measurements (Figure S11, Supporting Information) and the temperature coefficient of resistance (TCR) was estimated as shown in Figure S12 (Supporting Information). The magnitude of TCR was calculated using, TCR $= \frac{1}{R}\frac{dR}{dT} \times 100\%$, where R is the device resistance measured at different stage temperatures and T is the

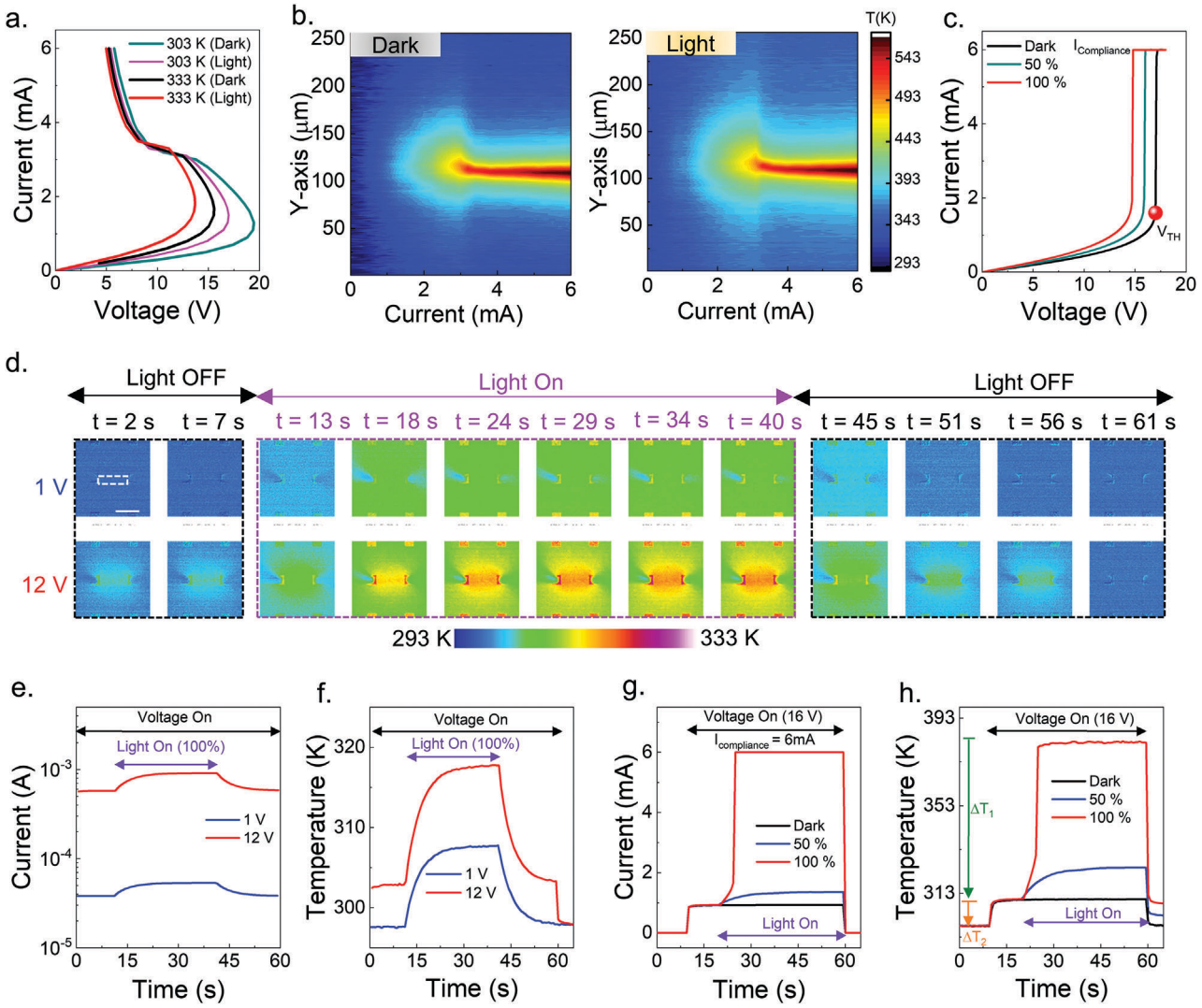

Figure 4. a) Current-controlled *I–V* data of a 120 μm device during in situ thermal mapping. b) 2D temperature maps as a function of device current under dark and white light illumination, obtained at middle of the device perpendicular to the direction of current flow. c) Voltage-controlled *I–V* data during in situ thermal mapping of a different device with similar characteristics. d) Temporal characteristics of in situ thermal maps recorded by applying constant bias voltages of 1 and 12 V, respectively. The illumination started at 13 s and then the light source was turned off at 42 s. e) Device current during light on–off events at different bias voltages. f) Corresponding mean temperature of the active device area (indicated by the white dashed line in the 2D map for $t = 2$ s). g,h) Device current and extracted mean temperature as a function of light intensity (with respect to power level) when biased with a fixed voltage (16 V) with magnitude near to the threshold voltage. The illuminance of the xenon lamp was around 1×10^6 lux when operated at an intensity of 100%.

stage temperature in Kelvin. The V_3O_5 device exhibited a TCR of around −2.66 (% K^{-1}) at room temperature, which is within the range of TCR reported for established bolometric materials, such as Bi_2O_2Se, α-Si and VO_x (between −1.6 and −4.77% K^{-1}).[7a,18a,22] The magnitude of TCR remains approximately constant for temperatures in the range from 303 to 363 K but increases as the temperature approached that of the IMT, as expected, reaching a value of −4.6% K^{-1} at 423 K. These data clearly identify a new bolometric material with high TCR and indicate its potential as a temperature-sensitive material for uncooled microbolometer application. Significantly, the sustained NDR response even above 400 K, along with the temperature-dependent change in resistance (as indicated by TCR values), clearly demonstrates that V_3O_5 possesses a much broader operating (temperature) range compared to VO_2.[7a] This characteristic positions V_3O_5 for various applications beyond the capability of VO_2 due to its lower IMT temperature, as previously mentioned.

2.4. Application of the Phototuneable Device Response in Neuromorphic Computing

2.4.1. A Light Sensitive Oscillation Neuron and the Utility of Spike Frequency Tuning in Image Segmentation

The utility of phototuneable NDR and threshold switching response were assessed by constructing a Pearson–Anson oscillator using the circuit configuration shown in **Figure** 5a. The device

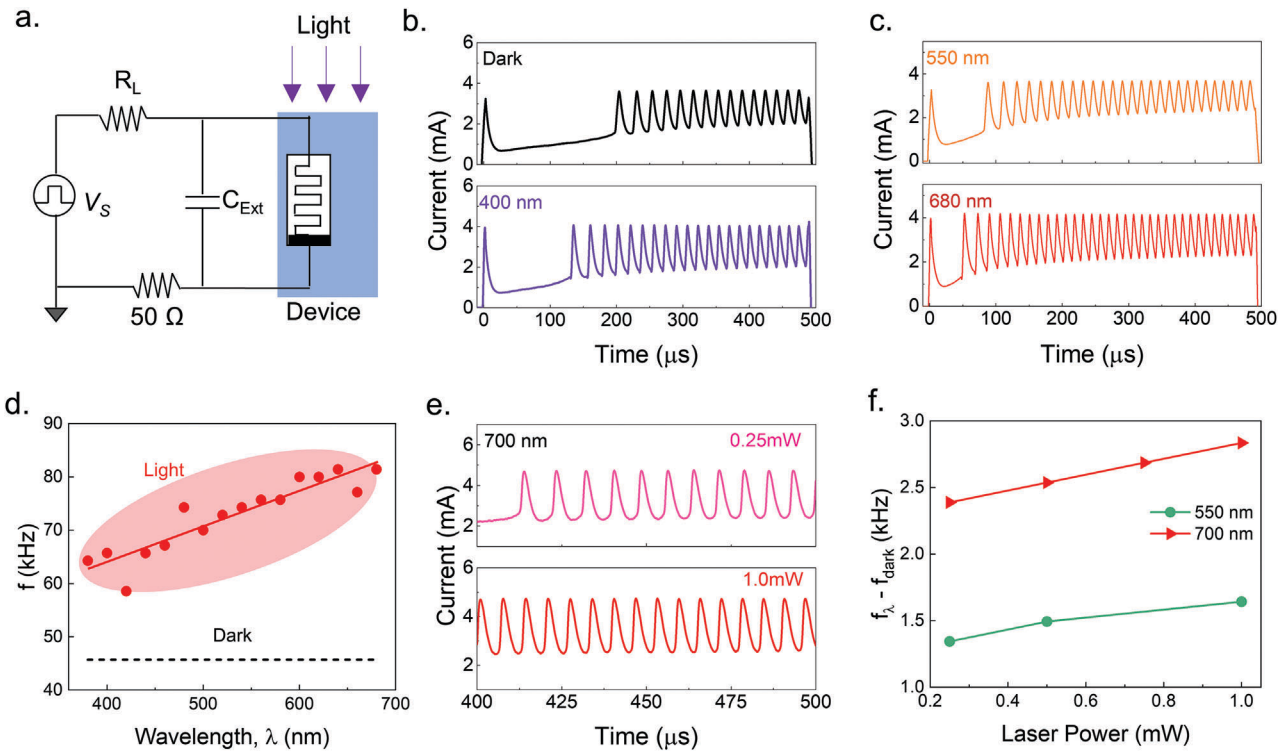

Figure 5. a) Circuit configuration used to measure oscillation dynamics. b,c) Measured oscillation waveforms under dark and illumination. d) Oscillation frequency as a function of wavelength, e) oscillation waveform measured under different light intensity for a fixed wavelength of 700 nm, and f) oscillation frequency as a function of light intensity.

exhibited self-sustained relaxation oscillation when a millisecond voltage pulse (V_S) was applied. The oscillation frequency was observed to depend on the source voltage V_S, load resistor, R_L, and parallel capacitor C_{Ext} (see Figure S13, Supporting Information), as expected.[3e]

As a significant advancement in the present study, we show that optical illumination can be used as a means of controlling the oscillation dynamics (Figure 5) of the memristor. Specifically, we found that the oscillation frequency can be determined by the light wavelength and incident light intensity as shown in Figure 5b–f.

For an Pearson–Anson oscillator, the frequency of oscillation can be expressed as:[23]

$$f = \frac{1}{\alpha R_L C \ln\left(\frac{V_S - V_H}{V_S - V_{TH}}\right)} \quad (2)$$

where α is a scaling factor and C is the device capacitance. This equation shows that oscillation frequency is a strong function of V_{TH} and V_H and can be modulated by tuning these parameters, as shown in Figure 5.

As demonstrated earlier, the NDR response can be tuned by the light intensity as well as the wavelength of the incoming light. This in turn leads to the reduction of threshold parameters that determines the oscillation frequency (further details are given in Figure S10, Supporting Information).

The ability to modify the oscillator dynamics or spiking rate using light-exposure is interesting as it can be used to eliminate the need of an external photodetector to control oscillation dynamics reported in recent studies[7b,14] and also provides the basis for constructing a sensory neuron for direct optical input into a neural network.

An example of this approach is shown in **Figure 6** where wavelength-guided image segmentation is demonstrated by simulating an array of oscillators, following a similar approach reported.[14] The input image is sensed and spike-encoded by the array of devices utilizing their sensitivity to different wavelengths and then segmented by a spiking neural network (SNN) as shown in Figure 6a. In this process, the color channels of the image are first converted to chromaticity-coordinates, which represent color without its brightness component. The CIE 1931 color-matching functions are then used to find corresponding wavelengths, which is a reasonable approximation for wavelengths within the visible spectrum.

When a voltage pulse is applied (according to Figure 5a), the wavelength and intensity of the incident color determines the spike firing frequency of each device. This is synonymous to how biological cone photoreceptor cells have tuning curves that vary with the wavelength of impinging stimuli,[24] and transmit spike trains to the primary visual cortex for early vision processing via the occipital lobe.[25] Each spike is integrated over time to generate a firing rate for each pixel which is illustrated in Figure 6a, and then filtered with a 5 × 5 convolutional kernel that attenuates spikes emitted by high firing frequencies. This has the benefit of inducing sparsity in the decoded output and can also be implemented by leaky integrate-and-fire (LIF) neurons.[26] The filtering process is illustrated in Figure 6b. The final spike rates are then

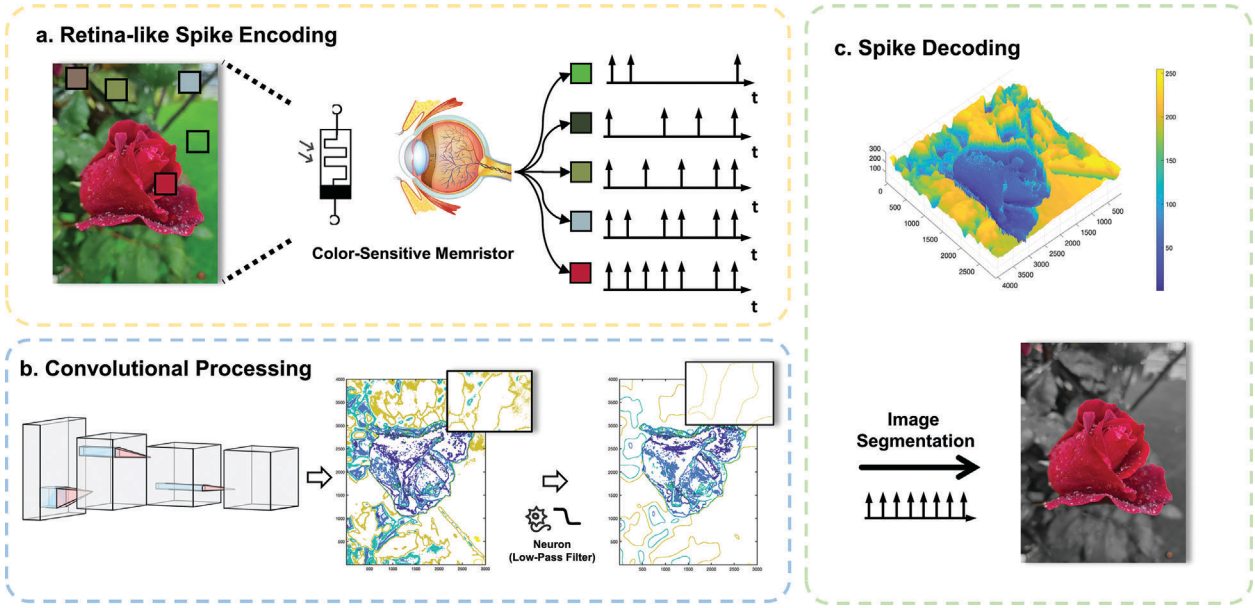

Figure 6. Image segmentation using photosensitive oscillatory dynamics. a) Retina-like spike encoding. The V_3O_5 oscillator converts incoming scenes into wavelength and intensity-modulated spike-trains. b) Convolutional processing: a basic series of kernels and spatial low-pass filtering is applied to the spike-trains to remove high frequency components. c) Spike decoding. Output firing frequencies are normalized back to the RGB spectrum.

decoded back to a final pixel intensity such that a segmentation mask can be constructed. A contour map of the firing rate of each device is shown in Figure 6c, where the low pass filtered firing rate is applied as a segmented mask to the original image. Firing rates that are filtered out block the background image from further downstream processing and are shown as the desaturated regions of the figure.

This feature of wavelength and intensity dependence on the current response of our device can be harnessed in furthering low-power deep learning models that suppress the transmission of pixels that do not contribute to downstream processing. Event-driven models, such as SNNs, can exploit this sparsity in sensory processing.[27]

In this context, it is important to note that the application of tunable NDR or threshold switching response is not limited to oscillation-based applications. They can also be used for other applications, including as a selector element for memory technology addressing sneak-path current problem.[6a,7a]

2.4.2. In-Sensor Reservoir Computing

The photosensing capabilities of our devices shown in Figure 3 can also be used for reservoir computing (RC) application, which is a framework for computation that may be viewed as an extension of neural networks. Typically used in time series prediction, RC employs a recurrent neural network (RNN) with a sparsely and randomly connected hidden layer, known as the reservoir. The reservoir transforms the input into a higher-dimensional space, which is then linearly combined to produce the output. The key advantage of RC is that only the output weights are trained, greatly simplifying the learning process, and reducing computational cost. This makes RC a powerful tool for tasks such as speech recognition, robot control, and many other applications where traditional RNNs are commonly used.[28,29]

The architecture of reservoir computing, as depicted in **Figure** 7a utilizes edge cropping and binarization techniques on the image dataset to generate an input sample size that is more compatible with the network.[16] This input sample is subsequently restructured into four data columns. Each row of data is then transformed into light pulses and incorporated into the device (as illustrated in Figure 3f), effectuating the modifications in the reservoir. The final step involves connecting to a multilayer perceptron (MLP) for classification purposes. Throughout the entire computational process, only the weights of the MLP layer are trained, significantly reducing the network training workload.

The classification results of the MNIST dataset, using this reservoir computing architecture, are presented in Figure 7b–d. Figure 7b displays the t-SNE (t-Distributed Stochastic Neighbor Embedding, a common method for data dimensionality reduction) plot of the MNIST test dataset after it has been processed by the reservoir layer. It is evident that the data exhibits excellent classification capabilities during post reservoir layer processing,[17] as compared to the dispersion between classes. Figure 7c represents the confusion matrix of the trained network for the entire MNIST test dataset. The network exhibits commendable classification accuracy across most categories, with the classification accuracy for the number "1" nearing 100%. The network training process's accuracy variation with each epoch is shown in Figure 7d. It is clear that the network demonstrates robust classification capabilities for the dataset after 1–2 epochs.

Finally, a comparison of the accuracy and computational effort of the currently employed reservoir computing and a single-layer artificial neural network (ANN) for the classification of MNIST data is shown in Figure 7e. It is observed that while the current classification accuracy of reservoir computing closely mirrors that of the single-layer ANN (with the classification accuracy

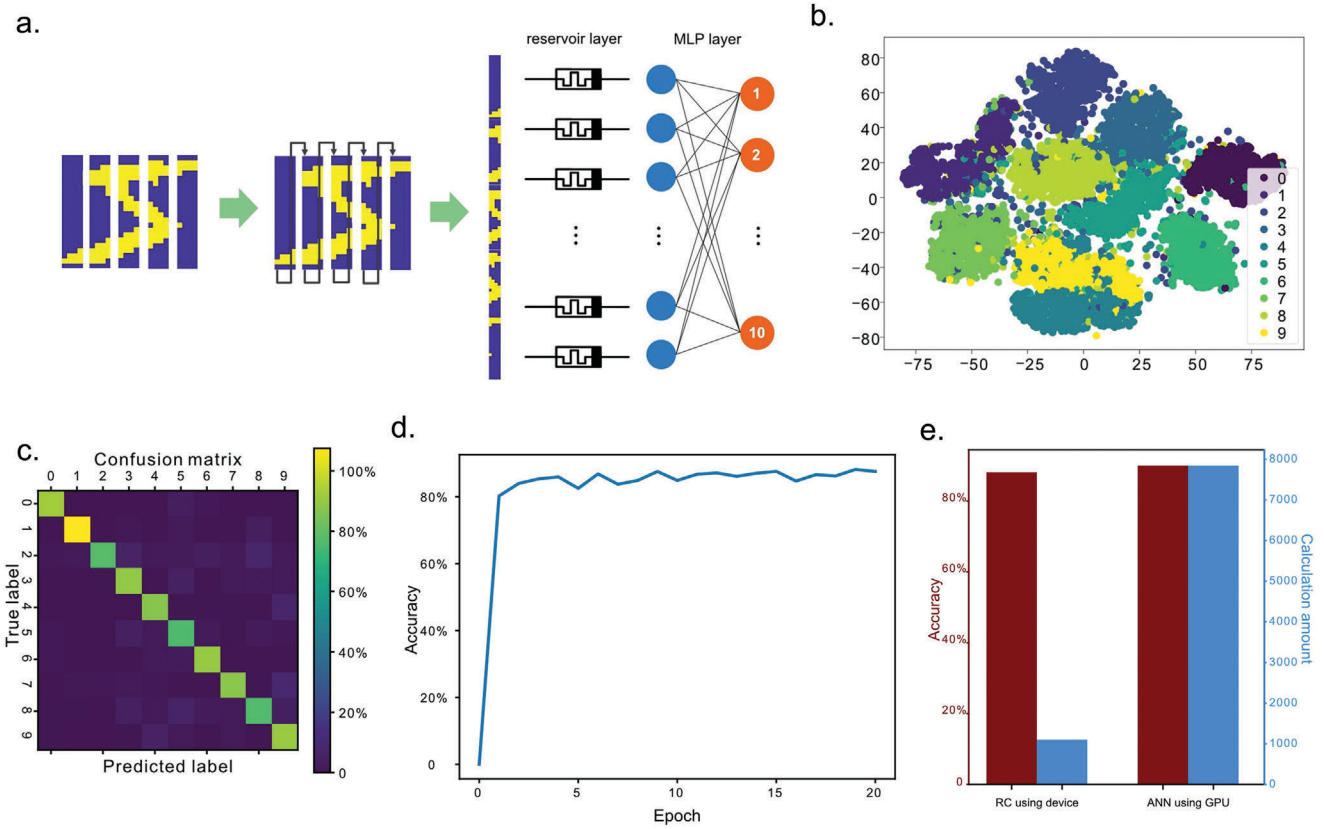

Figure 7. a) Architecture of reservoir computing (left: edge cropping, binarization and reshaping of image dataset; right: memristor-based neural network). b) *t*-Distributed Stochastic Neighbor Embedding (t-SNE) plot of the MNIST test dataset after processed by the reservoir layer (in the simulation, the time-resolved photocurrent data measured at 77 K with 10 s light exposure (Figure 3f) was used for the reservoir layer). c) Confusion matrix of the trained network for the entire MNIST test dataset, d) Accuracy variation of the network with each epoch. e) Comparison of accuracy and computational effort of currently used reservoir computing and single-layer artificial neural networks (ANN) for single image classification of MNIST data.

of reservoir computing at 89.4, and that of the single-layer ANN at 90.2), the computational effort is significantly reduced by a factor of seven. This indicates that the current computing architecture is not only conducive for devices, but it also significantly diminishes the network's computational load while nearing the classification accuracy's upper limit.

3. Conclusions

In summary, we have reported broad-band optical control of threshold switching parameters and electrical spikes in two terminal V_3O_5 devices when configured in Pearson–Anson oscillation circuit. The threshold and hold voltages and the oscillation frequency were shown to be regulated by illumination intensity and light wavelength due to a photoinduced decrease of device resistance. This is mediated by photoconductive and bolometric nature of the V_3O_5 film as inferred from conductive-AFM, in situ thermal imaging, and temperature-dependent electrical measurements. Additionally, using temperature-dependent resistance measurements, we reported a new bolometric material (V_3O_5) with TCR value as high as $-4.6\%\ K^{-1}$ at 423 K. Finally, using simulated device arrays we demonstrated the utility of optically tuned dynamical photoresponse and oscillation dynamics by showing its effectiveness in performing reservoir computing with reduced computational effort and image segmentation, respectively. Our demonstration of photoresponse and optically controlled oscillation dynamics without an external photodetector could be of use in the development of scalable, compact, and power efficient devices enabling direct optical input in SNNs, important for autonomous driving and robotic vision.

4. Experimental Section

Fabrication of V_3O_5 Devices: Planar, two-terminal metal-oxide-metal devices were fabricated using electron-beam lithography. V_3O_5 films of thickness ≈500 nm were deposited on glass slides, quartz, or thermally oxidized Si substrates using reactive sputter deposition with the substrate temperature kept at 873 K.[6b,9a] Metal electrodes were subsequently defined by electron-beam lithography, with the metal electrodes (200 nm Pt with a 5 nm Ti adhesion layer) deposited by successive e-beam evaporation. V_3O_5 films of the same thickness were also deposited onto 25 nm Pt-coated glass slides for through-film C-AFM measurements.

Material Characterization: The stoichiometry and crystal structures of the V_3O_5 films were analyzed by Rutherford back-scattering (RBS) and grazing incident X-ray diffraction (GI-XRD), respectively. The thickness, surface morphology, and chemical states of the films were measured by cross-sectional transmission electron microscopy (TEM), scanning electron microscopy (SEM), and X-ray photoelectron spectroscopy (XPS), respectively. The surface topography of the film was characterized by atomic force microscopy (Bruker AFM). The local current mapping and associated

responses of the V_3O_5 thin film under illuminations were measured by a customized C-AFM (Asylum Research, Oxford Instruments, combined with the diode laser, Omicron). The optical properties of the film were investigated using FTIR and UV–Visible spectroscopy. The local chemical composition of the oxide film between the two electrodes was investigated using a time-of-flight secondary ion mass spectroscopy (ToF-SIMS) equipment (IONTOF M6 (Germany)).

Device Characterization: Various electrical and optoelectronic measurements were conducted using an Agilent B1500A, a Keithley 4200SCS semiconductor parameter analyzer and an Agilent 2912A source meter. Base-line measurements were performed in air under dark conditions. The effect of illumination was determined by exposing devices to a set of laser light sources with wavelengths of 532, 635, 780, and 850 nm, respectively or to light from a fibre-coupled Fianium Supercontinuum laser within the wavelength range of 380 to 700 nm (laser spot size = 50 µm). The illumination power was measured by a power meter (Thorlabs, Inc.). Photoresponse time and the oscillation dynamics were measured using a Keysight MSO-X 4104A digital oscilloscope. In situ thermal maps of the device structure during electrical testing were recorded at different stage temperatures using InfraScope MWIR temperature mapping microscope employing an InSb detector (Quantum Focus Instruments Co.). A Xenon Light Source (MAX-303 VIS (385–740 nm)) was used as the excitation source during in situ thermal mapping and, a bandpass filter (385–740 nm) was used to limit the light intensity from the excitation source.

Statistical Analysis: To determine data uncertainties, we employed various techniques, including using instrument noise floor for single measurements such as continuous *I–V* sweeps and oscilloscope traces. Normalization of photocurrents was performed by setting the minimum and maximum magnitudes of currents to 0 and 1, respectively. Photocurrent decay time as a function of laser exposure time was fitted with a double exponential function in OriginLab softawere[30] as mentioned in the corresponding section of the manuscript. The mean ± SD threshold and hold voltage, and oscillation frequency were determined from successive five measurements. Averaging multiple measurements was effective in reducing uncertainties in these measurements. They were often too small to be visible relative to the plot scale.

Supporting Information

Supporting Information is available from the Wiley Online Library or from the author.

Acknowledgements

The authors would like to acknowledge access to NCRIS facilities and expertise at the ACT and WA nodes of the Australian National Fabrication Facility (ANFF) and the ANU ion-implantation Laboratory (iiLab) which is a node of the Heavy-Ion Accelerator (HIA) capability. S.K.N. acknowledges the support of Forrest Research Foundation in the form of Forrest Prospect Fellowship. C.V.M. and A.R. gratefully acknowledge the support from the National Science Foundation, through Award No. 2 033 328, and the Gordon and Betty Moore Foundation (Grant doi:10.37807/GBMF12250), and from the UPRM College of Arts and Science. X.S. acknowledges the support of John de Laeter Centre, Curtin University, and Curtin Faculty of Science and Engineering Research and Development Committee Small Grants. T.L. and Y.L. thank the Australian Research Council (ARC) for the funding support (DP200100159, FL210100017, DP230100462, and DE240100032).

Open access publishing facilitated by Australian National University, as part of the Wiley - Australian National University agreement via the Council of Australian University Librarians.

Conflict of Interest

The authors declare no conflict of interest.

Author Contributions

S.K.N. worked on conceptualization and project design, implementation, material characterization, electrical measurements, oscillation measurements, data analysis and interpretation, and liaising with collaborators and drafting the manuscript. S.K.D. worked on device fabrication, electrical measurements, data analysis, and LTSpice modeling. S.K. Nandi worked on device fabrication, data analysis, and interpretation, liaising with collaborators and supervision. C.V.M. and A.R. worked on thin film deposition, XRD, and resistivity measurements. C.X. and Z.W. worked on simulation and writing (reservoir computing). M.U. worked on MWIR temperature mapping. S.Z. worked on light-controlled electrical measurements. R.-J.Z. and J.E. worked on simulation and writing (spike encoding). X.S. worked on SIMS, SEM, and TEM measurements. S.K. Nandi, R.G.E., T.L. and Y.L. worked on conductive AFM. Y.B. and L.F. worked on preliminary photodetection measurements, and light-controlled oscillation measurements. N.S. worked on UV–Visible spectroscopy and XPS. W.P. performed FTIR. H.W worked on low temperature photocurrent measurements. W.L. and L.F. performed data interpretation and supervision. R.G.E. performed project oversight, supervision, RBS analysis, data interpretation, and drafting the manuscript.

Data Availability Statement

The data that support the findings of this study are available from the corresponding author upon reasonable request.

Keywords

bolometric material, negative differential resistance, neuromorphic computing, oscillation neuron, photomemristor, reservoir computing, threshold switching, V_3O_5, vanadium oxide

Received: January 17, 2024
Revised: March 18, 2024
Published online:

[1] a) M. Weiher, M. Herzig, R. Tetzlaff, A. Ascoli, T. Mikolajick, S. Slesazeck, *IEEE Trans. Circuits Syst. I: Regular Pap.* **2021**, *68*, 2082; b) A. Ascoli, M. Weiher, M. Herzig, S. Slesazeck, T. Mikolajick, R. Tetzlaff, *J. Low Power Electron. Appl.* **2022**, *12*, 22; c) A. Parihar, N. Shukla, M. Jerry, S. Datta, A. Raychowdhury, *Sci. Rep.* **2017**, *7*, 911.

[2] G. Csaba, W. Porod, *Appl. Phys. Rev.* **2020**, *7*, 011302.

[3] a) S. Kumar, R. S. Williams, Z. Wang, *Nature* **2020**, *585*, 518; b) D. Ielmini, *Microelectron. Eng.* **2018**, *190*, 44; c) J. M. Goodwill, D. K. Gala, J. A. Bain, M. Skowronski, *J. Appl. Phys.* **2018**, *123*, 115105; d) S. K. Nandi, S. Li, X. Liu, R. G. Elliman, *Appl. Phys. Lett.* **2017**, *111*, 202901; e) X. Liu, S. Li, S. K. Nandi, D. K. Venkatachalam, R. G. Elliman, *J. Appl. Phys.* **2016**, *120*, 124102; f) X. Zhang, W. Wang, Q. Liu, X. Zhao, J. Wei, R. Cao, Z. Yao, X. Zhu, F. Zhang, H. Lv, *IEEE Electron Device Lett.* **2017**, *39*, 308.

[4] a) A. Pergament, A. Velichko, M. Belyaev, V. Putrolaynen, *Phys. Rev. B: Condens. Matter* **2018**, *536*, 239; b) N. Shukla, S. Datta, A. Parihar, V. Narayanan, A. Raychowdhury, presented at CNNA 2016; 15th International Workshop on Cellular Nanoscale Networks and their Applications, Dresden, Germany, August **2016**.

[5] a) M. D. Pickett, G. Medeiros-Ribeiro, R. S. Williams, *Nat. Mater.* **2013**, *12*, 114; b) S. K. Nandi, S. K. Nath, A. E. El-Helou, S. Li, T. Ratcliff, M. Uenuma, P. E. Raad, R. G. Elliman, *ACS Appl. Mater. Interfaces* **2020**, *12*, 8422.

[6] a) T. D. Dongale, G. U. Kamble, D. Y. Kang, S. S. Kundale, H.-M. An, T. G. Kim, *Phys. Status Solidi RRL* **2021**, *15*, 2100199; b) S. K.

Das, S. K. Nandi, C. V. Marquez, A. Rúa, M. Uenuma, E. Puyoo, S. K. Nath, D. Albertini, N. Baboux, T. Lu, *Adv. Mater.* **2023**, *35*, 2208477.

[7] a) Y. Zhang, X. Wang, Y. Zhou, H. Lai, P. Liu, H. Chen, X. Wang, W. Xie, *Nano Lett.* **2021**, *22*, 485; b) C. Chen, Y. He, H. Mao, L. Zhu, X. Wang, Y. Zhu, Y. Zhu, Y. Shi, C. Wan, Q. Wan, *Adv. Mater.* **2022**, *34*, 2201895; c) M. Son, J. Lee, J. Park, J. Shin, G. Choi, S. Jung, W. Lee, S. Kim, S. Park, H. Hwang, *IEEE Electron Device Lett.* **2011**, *32*, 1579; d) J. A. Rupp, M. Querré, A. Kindsmüller, M.-P. Besland, E. Janod, R. Dittmann, R. Waser, D. J. Wouters, *J. Appl. Phys.* **2018**, *123*, 044502; e) D. S. Jeon, T. D. Dongale, T. G. Kim, *J. Alloys Compd.* **2021**, *884*, 161041; f) J.-G. Ramírez, R. Schmidt, A. Sharoni, M. Gomez, I. K. Schuller, E. J. Patiño, *Appl. Phys. Lett.* **2013**, *102*, 063110.

[8] A. Beaumont, J. Leroy, J.-C. Orlianges, A. Crunteanu, *J. Appl. Phys.* **2014**, *115*, 154502.

[9] a) N. Kumar, A. Rúa, J. Lu, F. Fernández, S. Lysenko, *Phys. Rev. Lett.* **2017**, *119*, 057602; b) S. M. Bohaichuk, S. Kumar, G. Pitner, C. J. McClellan, J. Jeong, M. G. Samant, H.-S. P. Wong, S. S. Parkin, R. S. Williams, E. Pop, *Nano Lett.* **2019**, *19*, 6751.

[10] C. Adda, M.-H. Lee, Y. Kalcheim, P. Salev, R. Rocco, N. M. Vargas, N. Ghazikhanian, C.-P. Li, G. Albright, M. Rozenberg, *Phys. Rev. X* **2022**, *12*, 011025.

[11] T. S. Bhat, C. C. Revadekar, S. S. Patil, T. D. Dongale, D.-k. Kim, P. S. Patil, *J. Mater. Sci.: Mater. Electron.* **2020**, *31*, 10919.

[12] S. T. Killedar, N. A. Ahir, P. J. Morankar, A. P. Tiwari, P. B. Patil, T. D. Dongale, D.-k. Kim, *Opt. Mater.* **2020**, *109*, 110333.

[13] a) M. Kumar, S. Abbas, J. Kim, *ACS Appl. Mater. Interfaces* **2018**, *10*, 34370; b) F. Zhou, Y. Chai, *Nat. Electron.* **2020**, *3*, 664.

[14] Q. Wu, B. Dang, C. Lu, G. Xu, G. Yang, J. Wang, X. Chuai, N. Lu, D. Geng, H. Wang, *Nano Lett.* **2020**, *20*, 8015.

[15] F. Chudnovskii, E. Terukov, D. Khomskii, *Solid State Commun.* **1978**, *25*, 573.

[16] C. S. Lau, S. Das, I. A. Verzhbitskiy, D. Huang, Y. Zhang, T. Talha-Dean, W. Fu, D. Venkatakrishnarao, K. E. Johnson Goh, *ACS Nano* **2023**, *17*, 9870.

[17] P. Chen, X. Zhang, Z. Wu, Y. Wang, J. Zhu, Y. Hao, G. Feng, Y. Sun, T. Shi, M. Wang, *IEEE Trans. Electron Devices* **2022**, *69*, 2391.

[18] a) H. Yang, C. Tan, C. Deng, R. Zhang, X. Zheng, X. Zhang, Y. Hu, X. Guo, G. Wang, T. Jiang, *Small* **2019**, *15*, 1904482; b) F. Koppens, T. Mueller, P. Avouris, A. Ferrari, M. Vitiello, M. Polini, *Nat. Nanotechnol.* **2014**, *9*, 780.

[19] S. K. Nandi, E. Puyoo, S. K. Nath, D. Albertini, N. Baboux, S. K. Das, T. Ratcliff, R. G. Elliman, *ACS Appl. Mater. Interfaces* **2022**, *14*, 29025.

[20] G. A. Gibson, *Adv. Funct. Mater.* **2018**, *28*, 1704175.

[21] M. E. Itkis, F. Borondics, A. Yu, R. C. Haddon, *Stem Cells Int* **2006**, *312*, 413.

[22] P. K. Yadav, I. Yadav, B. Ajitha, A. Rajasekar, S. Gupta, Y. A. K. Reddy, *Sens. Actuators, A* **2022**, *342*, 113611.

[23] L. Gao, P.-Y. Chen, S. Yu, *Appl. Phys. Lett.* **2017**, *111*, 103503.

[24] a) A. Stockman, D. I. A. MacLeod, N. E. Johnson, *J. Opt. Soc. Am. A* **1993**, *10*, 2491; b) J. K. Eshraghian, K. Cho, C. Zheng, M. Nam, H. H.-C. Iu, W. Lei, K. Eshraghian, *IEEE Trans. Very Large Scale Integr. VLSI Syst.* **2018**, *26*, 2816.

[25] a) B. A. Wandell, J. Winawer, K. N. Kay, *Hum. Brain Mapp.* **2015**, *651*, 659; b) B. A. Wandell, S. O. Dumoulin, A. A. Brewer, *Neuron* **2007**, *56*, 366.

[26] H. Scharstein, *J Math Biol* **1979**, *8*, 403.

[27] J. K. Eshraghian, M. Ward, E. O. Neftci, X. Wang, G. Lenz, G. Dwivedi, M. Bennamoun, D. S. Jeong, W. D. Lu, *Proc. IEEE* **2023**, *111*, 1016.

[28] Z. Qi, L. Mi, H. Qian, W. Zheng, Y. Guo, Y. Chai, *Adv. Funct. Mater.* **2023**, *33*, 2306149.

[29] X. Wu, S. Wang, W. Huang, Y. Dong, Z. Wang, W. Huang, *Nat. Commun.* **2023**, *14*, 468.

[30] *OriginLab Corporation*, Northampton, MA, USA **2022**.